RESEARCH ARTICLE

Key Points:
- Low velocities in the crust delineate the magmatic plumbing system beneath Askja volcano in Iceland
- Primary magma storage region is at a depth of 5 km bsl but extends into the lower crust where melt movement generates microearthquakes
- Melt is distributed in discrete regions throughout the crust to depths of over 20 km

Supporting Information:
- Supporting Information S1
- Movie S1
- Movie S2

Correspondence to:
T. Greenfield,
tg286@cam.ac.uk

The magmatic plumbing system of the Askja central volcano, Iceland, as imaged by seismic tomography

Tim Greenfield[1], Robert S. White[1], and Steven Roecker[2]

[1]Bullard Laboratories, University of Cambridge, Cambridge, UK, [2]Rensselaer Polytechnic Institute, Troy, New York, USA

Abstract The magmatic plumbing system beneath Askja, a volcano in the central Icelandic highlands, is imaged using local earthquake tomography. We use a catalog of more than 1300 earthquakes widely distributed in location and depth to invert for the P wave velocity (V_p) and the V_p/V_s ratio. Extensive synthetic tests show that the minimum size of any velocity anomaly recovered by the model is ~4 km in the upper crust (depth < 8 km below sea level (bsl)), increasing to ~10 km in the lower crust at a depth of 20 km bsl. The plumbing system of Askja is revealed as a series of high-V_p/V_s ratio bodies situated at discrete depths throughout the crust to depths of over 20 km. We interpret these to be regions of the crust which currently store melt with melt fractions of ~10%. The lower crustal bodies are all seismically active, suggesting that melt is being actively transported in these regions. The main melt storage regions lie beneath Askja volcano, concentrated at depths of 5 km bsl with a smaller region at 9 km bsl. Their total volume is ~100 km^3. Using the recorded waveforms, we show that there is also likely to be a small, highly attenuating magmatic body at a shallower depth of about 2 km bsl.

1. Introduction

Seismic tomography has been used successfully at many volcanoes around the world [e.g., *Cardaci et al.*, 1993; *Lees*, 2007; *Lin et al.*, 2014] and provides an important constraint on the amount of melt stored below a volcano and, therefore, its potential hazard. Several tomographic studies have been made of Icelandic volcanoes including Krafla [*Arnott and Foulger*, 1994; *Schuler et al.*, 2015], Hengill [*Foulger et al.*, 1995], Katla [*Gudmundsson et al.*, 1994], and Grimsvötn [*Alfaro et al.*, 2007]. Here we report results from a seismic tomographic study of the active Askja volcano in Iceland using body waves.

Askja is located at the southern end of the Northern Volcanic Zone (NVZ, Figure 1 inset), which marks the location of the plate spreading boundary between the North American and Eurasian plates where it passes through Iceland. Askja is one of five volcanic systems in the NVZ. The eponymous Askja volcanic system stretches northward more than 60 km from the Vatnajökull icecap (see Figure 1 for location) and is one of the largest volcanic systems in Iceland [*Sæmundsson*, 1979; *Thordarson and Larsen*, 2007]. Due to its remoteness, Askja was not known to be active until 1875 when it erupted with a spectacular plinian eruption which formed the most recent caldera, Öskjuvatn (Figure 1) [*Brandsdóttir*, 1992; *Hartley and Thordarson*, 2012]. This activity was accompanied by eruptions to the north of Askja within the Askja volcanic system [*Hartley and Thordarson*, 2013]. Another series of significantly smaller eruptions occurred from Askja in the early part of the twentieth century. These were mostly focused around the newly formed Öskjuvatn caldera. Askja's most recent eruption was in 1961 when a 2 km long fissure opened on the north side of the volcano and erupted for 5 weeks [*Thorarinsson*, 1962].

Despite its remote location, the surface deformation of Askja has been measured almost every year since 1968 [*de Zeeuw-van Dalfsen et al.*, 2013]. The measurements were initially made using tiltmeters, but more recently, GPS and interferometric synthetic aperture radar techniques have been used. This has revealed that Askja has been subsiding since 1983, most likely due to cooling and contraction of a shallow body and plate spreading processes [*de Zeeuw-van Dalfsen et al.*, 2013].

Although Askja is currently subsiding and has not erupted for over 50 years, it was, until the 2014 Bárðarbunga-Holuhraun eruption, the most seismically active volcano in Iceland. This is because there is an active geothermal area located within Öskjuvatn and a series of left-lateral strike-slip faults located around the table mountain Herðubreið to the north (see Figure 1 for location) [*Green et al.*, 2014]. There are also multiple repeating earthquakes in the usually ductile lower crust beneath the Askja volcanic segment. These are interpreted to be caused by the movement of melt through the lower crust [*Soosalu et al.*, 2010; *Key et al.*, 2011a, 2011b; *Greenfield and White*, 2015].
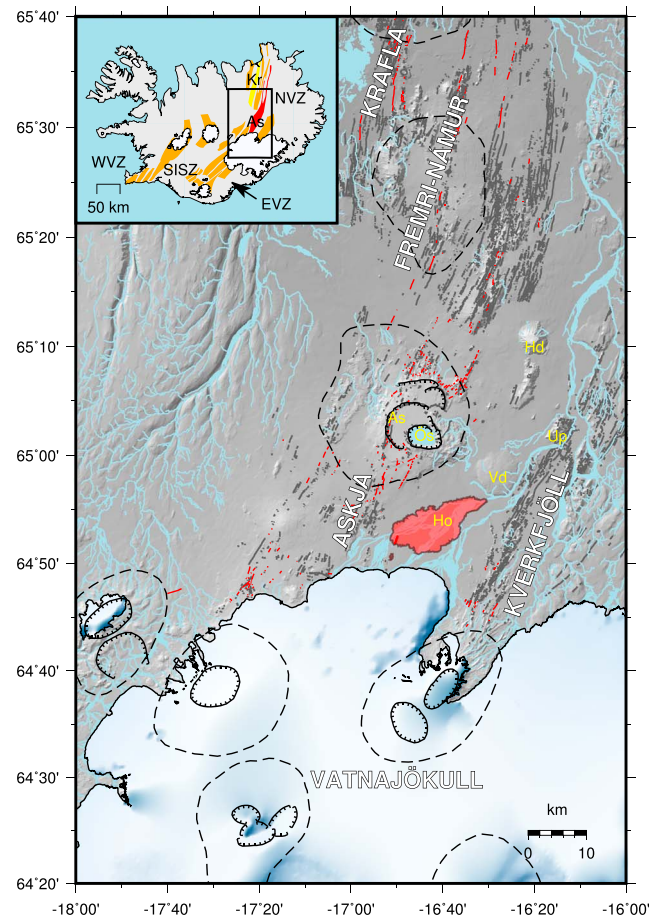
Figure 1. Map of the study area in northern Iceland. Central volcanoes are indicated by the dashed lines. Mapped calderas are shown as ticked lines. The Askja central volcano (As), the caldera lake Öskjuvatn (Ös), the table mountain Herðubreið (Hd), Upptyppingar volcano (Up), Vaðalda shield volcano (Vd), and the Holuhraun lava field (Ho) are labeled in yellow. The Askja, Kverkfjöll, Fremri-Námur, and Krafla volcanic systems are labeled in white and aligned with the rift axis. The Vatnajökull icecap is labeled in white. Black and red lines show mapped fractures and eruptive fissures respectively of *Hjartardóttir and Einarsson* [2015] and delineate the active rifts. Inset shows the location of the study area in Iceland (black box) along with the three neovolcanic zones: Western Volcanic Zone (WVZ), Eastern Volcanic Zone (EVZ), and the Northern Volcanic Zone (NVZ). The South Iceland Seismic Zone (SISZ), Askja volcanic system (As), and Krafla volcanic system (Kr) are all labeled.

The *P* wave velocity (V_p) structure of the Askja region was reported by *Mitchell et al.* [2013]. A large low-velocity region was imaged at a depth of 8 km below sea level (bsl) and interpreted to be the primary magma chamber of Askja. However, because there was a limited distribution of earthquakes and seismic stations, regions to the south of Askja and below 10 km depth were not well imaged. In this study, we use a denser network of three-component seismometers deployed around Askja and a larger and more spatially distributed catalog of earthquakes including those used by *Mitchell et al.* [2013] to image V_p and the V_p/V_s ratio in the subsurface. This significantly improves the images from *Mitchell et al.* [2013] and allows us to interpret the magmatic plumbing system from midcrustal depths (20 km bsl) to the surface.

2. Data Set and Method

2.1. Seismic Network

We have deployed and operated a dense network of seismometers around Askja and the surrounding region continuously since 2008. The network is composed primarily of between 20 and 40 Guralp CMG-6TDs (30 s) and augmented with up to 5 Guralp CMG-ESPCDs (60 s), 2 Guralp CMG-3Ts (120 s) with Nanometrics Taurus data loggers, and three stations operated by the Icelandic Meteorological Office. All instruments record at 100 samples per second throughout the year except for eight instruments with only 4 GB of internal storage that recorded at 50

samples per second. To maximize data coverage, we moved approximately one third of the network each year to new locations. By only moving a part of the network we maintain the high quality and stability of the network while increasing the number of station locations we can use in the inversion to 120. This has resulted in an average station spacing of ~5 km.

2.2. Earthquake Catalog

Earthquakes were automatically detected and located using Coalescence Microseismic Mapping (CMM) [*Drew et al.*, 2013]. This continually migrates an onset function derived from the raw seismic data through a predefined velocity model to find the best fitting location and origin time of the energy released by an earthquake. The onset function is generated by filtering and demeaning the data and then calculating the average amplitude in a short window (0.2 s) and a long window (1 s). The windows are slid along the seismic trace for each component and divided to create the short-term-average (STA) over long-term-average (LTA)
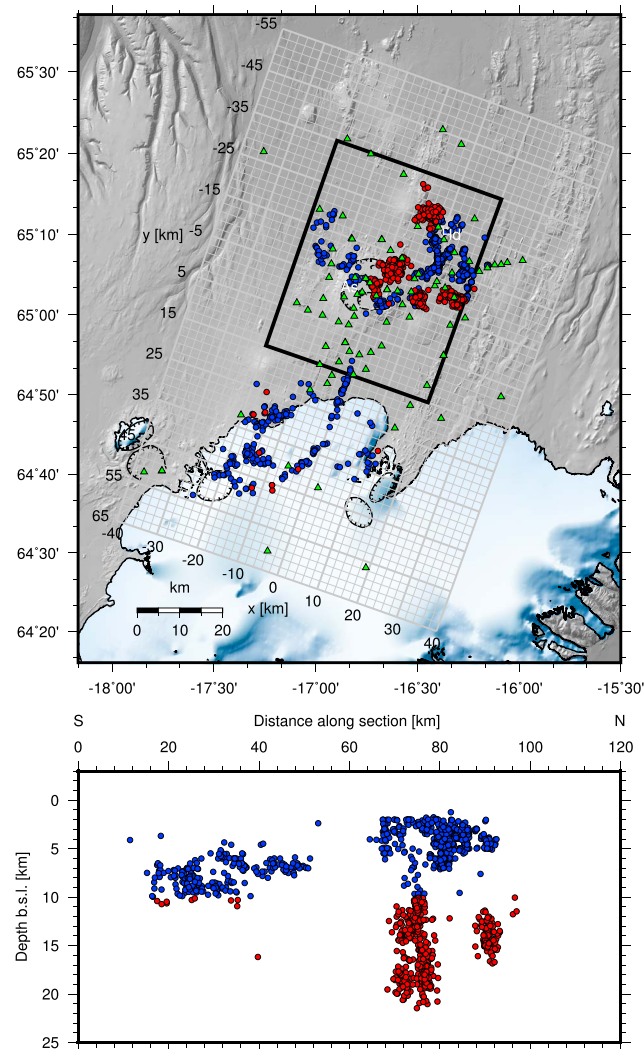
Figure 2. Earthquake location and tomographic grid. Earthquakes shallower than 10 km are indicated by blue circles; earthquakes deeper than 10 km are indicated by red circles. Askja (As) and Herðubreið (Hd) are labeled in white. The stations used in the tomographic inversion are indicated by the green triangles. The tomographic grid is shown as grey lines with 2 km spacing oriented parallel to the plate spreading direction. The area of interest is indicated by the thick black rectangle.

onset function (STA/LTA). Earthquakes are detected if this function exceeds a value greater than 2. The resulting catalog for the Askja region in the period 2009–2015 consists of more than 30,000 earthquakes.

In general, the arrival time picks using the CMM method are usually slightly later than the first onset of the *P* or *S* phase. Therefore, we have manually refined the arrival time picks for more than 3000 earthquakes chosen to give good spatial and depth coverage of the region (Figure 2). We do this by altering the automated arrival time pick made by CMM by hand to match the arrival time of the *P* wave on the vertical component and the *S* wave on the two horizontal components. Typically, the events contain impulsive *P* and *S* wave arrivals which can be picked to an accuracy of 0.01 s and 0.02 s, respectively (Figure 3). Importantly, the Bárðarbunga-Holuhraun dike intrusion during 2014–2015 [*Green et al.*, 2015; *Sigmundsson et al.*, 2015; *Ágústsdóttir et al.*, 2016] produced many earthquakes, up to local magnitudes of 5 south of Askja, in a previously seismically quiet area. Inclusion of these earthquakes dramatically improves the tomographic velocity model by increasing the spatial coverage and number of crossing raypaths.

The manually refined earthquakes were relocated using NonLinLoc [*Lomax et al.*, 2000], a probabilistic earthquake location algorithm using the equal differential time formulation of *Font et al.* [2004]. We use the 1-D seismic velocity model derived by *Mitchell et al.* [2013] from

local earthquakes around Askja to locate the events. From this catalog we have selected 1363 earthquakes (~42,000 arrival times) which each have more than eight arrival time picks and a root-mean-square residual misfit of less than 0.25 s as an input into the tomographic inversion (Figure 2).

2.3. Tomographic Method

We use the tomographic inversion method of *Roecker et al.* [2006], previously used to image the 3-D velocity structure of the San Andreas fault near Parkfield [*Roecker*, 2004], Western Tibet [*Nunn et al.*, 2014], and more recently, the Krafla central volcano north of Askja [*Schuler et al.*, 2015]. The key feature of the *Roecker et al.* [2006] method is that the traveltimes are generated using a finite difference (FD) solution to the eikonal equation [*Vidale*, 1988; *Hole and Zelt*, 1995]. The advantage of the FD technique is increased accuracy in a highly heterogeneous medium, as expected in a volcanic region, and less ambiguity in determining the global traveltime minima.
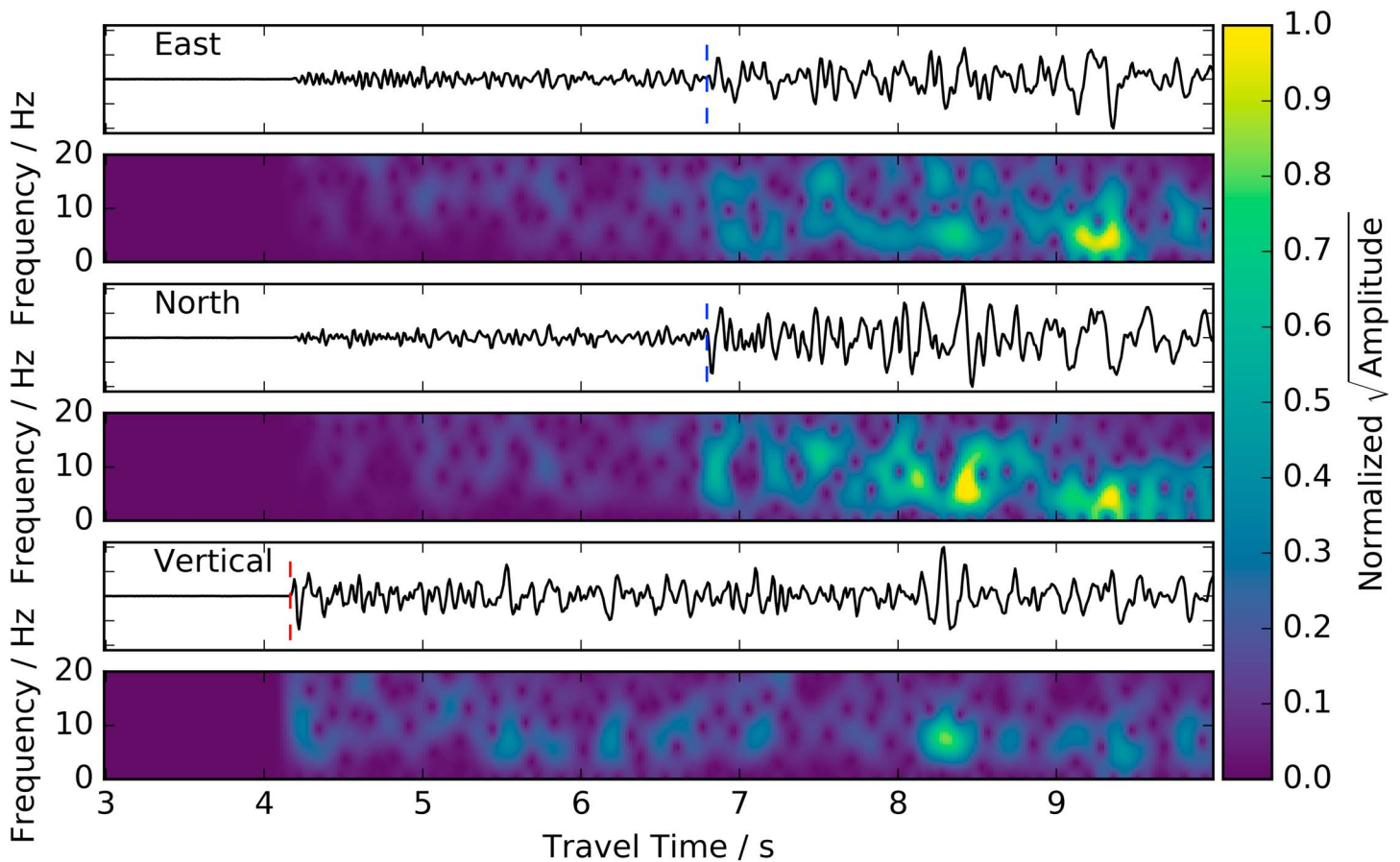
Figure 3. Typical three-component seismograms of an earthquake recorded by the seismic network around Askja. *P* and *S* wave arrival times have been picked by hand and are indicated by the red and blue lines, respectively. The frequency content of the earthquake is displayed in the spectrogram below each seismogram and colored by the square-root of the amplitude, normalized over all traces, as indicated by the color bar on the right.

Traveltimes are calculated on a $120 \times 80 \times 38$ km 3-D Cartesian grid (Figure 2) with a grid spacing of 500 m, and intragrid times are estimated by trilinear interpolation. The grid is created using the Universal Transverse Mercator map projection and then rotated 19° to be aligned with the regional spreading direction. The spatial extent of the grid is chosen such that all the earthquakes in the catalog and all the seismic stations are enclosed within the grid (Figure 2). Some buffer space is included to avoid edge effects when calculating the traveltime look-up table or locating earthquakes. The 500 m grid spacing is well below the expected resolution of the model and produces accurate traveltimes while ensuring that the calculation is computationally tractable.

The choice of starting model can have an influence on the final model. To test this, we randomly vary the model of *Mitchell et al.* [2013] used to generate the earthquake catalog. No significant differences in the main anomalies were found, suggesting that in this case, the effect of the starting model is small. We therefore use the 1-D velocity model of *Mitchell et al.* [2013] as a starting model. Earthquakes are located within the traveltime grid by an efficient grid search to a subgrid with a grid spacing of 0.5 m. Raypaths from each source to each receiver are determined by marching backward along the steepest traveltime gradient. Residuals between theoretical and observed traveltimes are then generated for each observation.

Partial derivatives are calculated on the fine grid, but it is not useful to have each grid point as an independent variable when it comes to the inversion stage. Therefore, before inversion the derivatives are accumulated onto a coarse grid with a grid spacing of 2 km in the *x* and *y* directions (Figure 2). In the *z* (vertical) direction, to improve resolution and lessen the dependence of final model on the fixed location of the grid points, we use a spacing of 1 km below 20 km bsl and 0.5 km elsewhere.
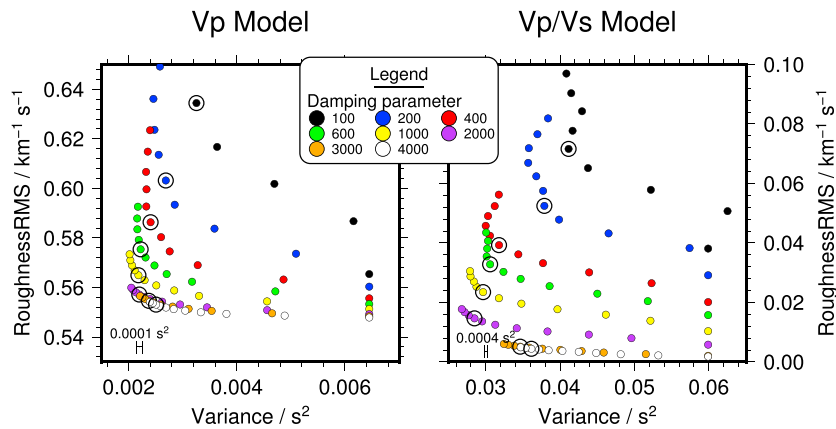
Figure 4. The variation in the misfit with model roughness for each model (V_p and V_p/V_s) with a range of damping factors (100–4000 $s^2 km^{-2}$). Each run with a different damping parameter is indicated by a different color, and each iteration within each run is marked by a colored circle, increasing from right to left. The chosen iteration for each model is indicated by the circled circle. The chosen damping parameter is 2000 $s^2 km^2$ and is indicated by the purple circles. The circled iteration for this run has the smallest misfit of any run. The expected misfit given the errors on the data is indicated by the error bar in the lower left corner of each plot.

We invert for V_p and V_p/V_s directly and infer V_s from those models, partly because of the interpretive usefulness of V_p/V_s, but also because estimates of V_p/V_s derived from ratios of V_p and V_s models suffer from inconsistencies in resolution due to the differing coverage of the P and S waves. V_p/V_s derivatives are calculated in the expansion of S wave arrival times using the chain rule [*Roecker*, 2004], but because of the difference in units the magnitudes of these V_p/V_s derivatives are generally about a factor of 10 less than those for V_p. This difference can lead to an unrealistic suppression of perturbations to the V_p/V_s model. To mitigate this difference in scaling between V_p and V_p/V_s, we weight the V_p/V_s derivatives by a factor of 10.

Inversion is performed using the LSQR algorithm [*Paige and Saunders*, 1982], and the resulting perturbations are then smoothed using a moving window of three grid points in each direction. Importantly, even though we relocate the hypocenters at each iteration, we invert for both the hypocenters and the wave speed and so avoid potential biases generated by only inverting for the wave speed model.

The LSQR algorithm uses a single damping parameter, which can have a significant effect on the final solution. Ideally, the damping parameter chosen should result in the best fitting, smooth model in a minimum number of iterations. We tested a range of damping parameters from 10 to 4000 to fully explore the effect of this important parameter (Figure 4). Within each run we select the final iteration (circled dots in Figure 4) to be the smoothest model (calculated by the root-mean-square second derivative), such that any further reduction in variance is less than the anticipated variance given the errors in the observations (error bars in Figure 4). This is near the corner of a misfit versus roughness plot (Figure 4) and means that we try to avoid fitting noise in the model.

As may be expected, we find that large damping parameters result in overly smooth models and require many iterations to reach the final model, whereas low values of the damping parameters do not converge to a smooth model. The optimal damping parameter was chosen to be 2000 $s^2 km^{-2}$, as this produces a model with the smallest overall misfit (Figure 4). From an initial data variance of 0.3564 s^2 the 3-D model reduces the variance by 99% (0.0034 s^2). This suggests that the initial 1-D model is a poor fit to the data and that the region of crust beneath Askja is highly heterogeneous. The expected variance given the uncertainties in the data is 0.0002 s^2, an order of magnitude smaller than the variance of the final model. This indicates that while there may be further unmodeled structure in the data, the model is probably not fitting noise.

3. Synthetic Tests: Checkerboard

We use checkerboard tests to assess the minimum possible size of a detectable velocity anomaly using the grid spacing, earthquake locations, and seismic network of the observed data. Synthetic checkerboard velocity models with alternating positive and negative anomalies (±2.7% V_p and ±5 V_p/V_s relative to the initial 1-D model) are created with a variety of sizes (from 10 km to 2 km). Synthetic arrival times are then generated
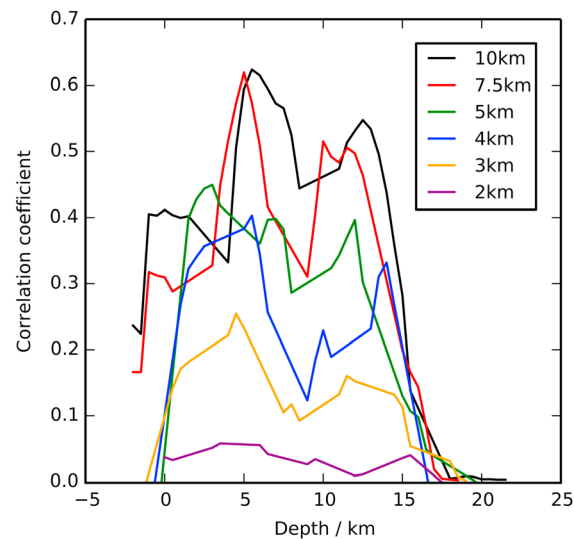
Figure 5. Variation in the cross correlation between the input synthetic checkerboard model and the recovered model at each depth for six different sized checkers: 10 km (black), 7.5 km (red), 5 km (green), 4 km (blue), 3 km (orange) and 2 km (purple).

for every observation using the final earthquake locations from the inversion with the real data. The synthetic data are then inverted using the same parameters as the inversion using real data. Importantly, we allow the locations and origin times of the earthquakes to vary when inverting the synthetic data in order to minimize their travel time residual.

The checkerboard tests show how well we can recover an initial checkerboard-like velocity model using the network and earthquakes used in the actual inversion. However, it is important to understand the limitations of this technique, especially those areas of potential uncertainty that are not included in the analysis [*Rawlinson e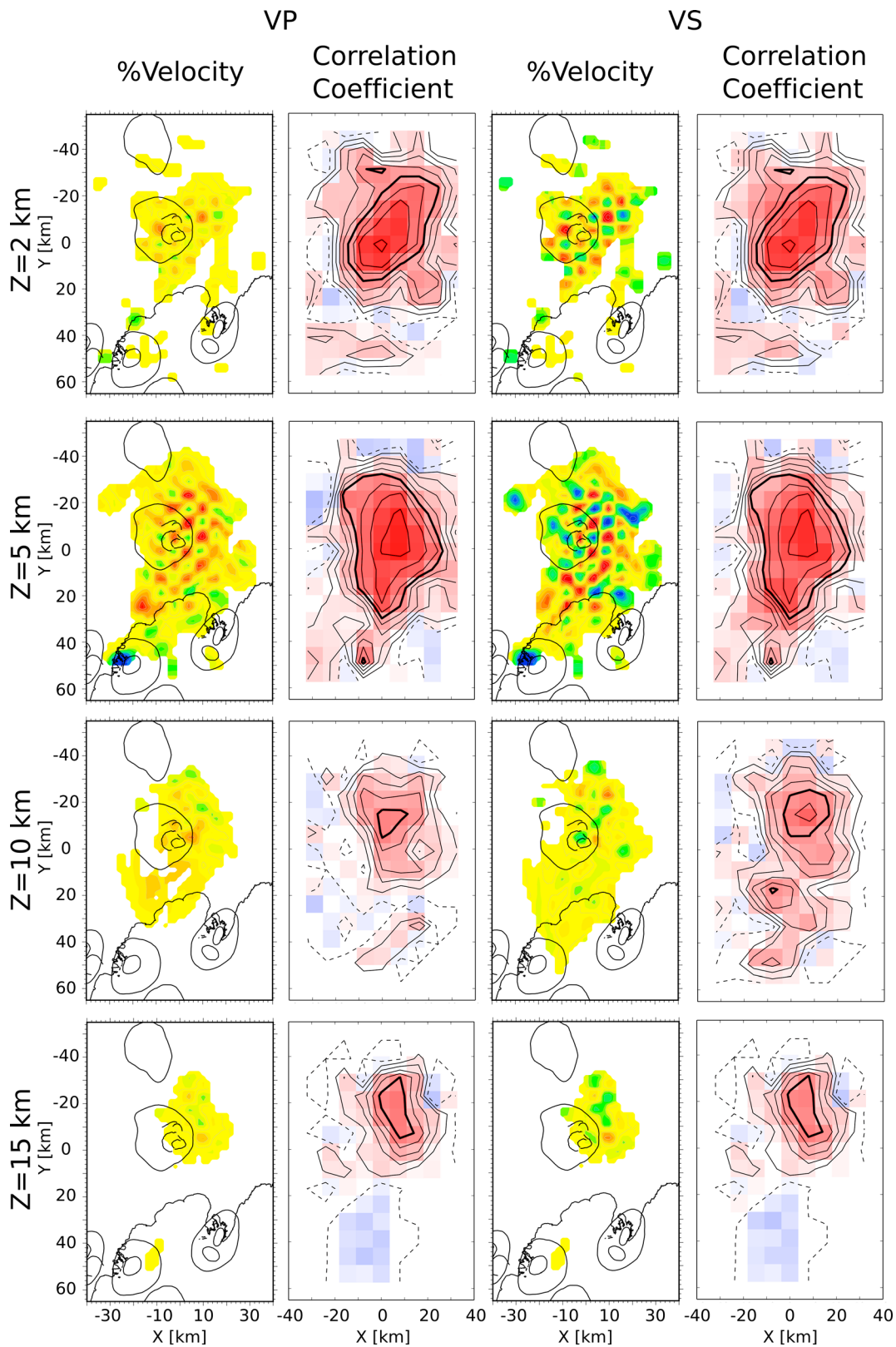t al.*, 2014]. For example, although we add Gaussian noise to the synthetic arrival times using the same error as reported in the real data, we do not test whether or not that error is representative of the true noise in the arrival time data set. Additionally, we use the same forward problem solver for both the synthetic arrival time generation and during the inversion process. This removes any potential errors in the calculation of the arrival times. Finally, the checkerboard model is so different from the true model that the raypaths in the checkerboard model and in the true model may be different, possibly resulting in areas of the checkerboard model being illuminated where there are no raypaths in the true data set and vice versa. Because of these limitations, we avoid overinterpreting the checkerboard tests and perform further synthetic tests using more realistic geometries in section 5.

Checkerboard tests are commonly interpreted qualitatively by visually comparing the input and output models. In an effort to be more quantitative we have masked out regions of the input model that do not have rays crossing them and then cross correlated each 2-D depth slice with the corresponding depth slice from the final output model. The resulting single correlation value is a quantitative estimate of the degree to which the output model matches the input model.

Figure 5 shows the results from the cross-correlation analysis. An abrupt drop in the cross-correlation values from ~0.5 to ~0 occurs between 4 km-sized checkers and 2 km-sized checkers. We interpret this to indicate that the minimum recoverable sized feature is ~4 km across. However, due to variability in source and station distribution, the resolution is likely to be better in certain areas than others. To assess this, we have cross correlated the input and output models within a sliding square window with sides twice the length of the checker size. This technique reveals areas where the input model is well recovered. By contouring this data set, we have selected regions of the grid where we have sufficient confidence to show well-recovered features (Figure 6). The regions delineated in this way with a correlation coefficient greater than 0.5 are displayed in Figure 7.

4. Results

Sections through the final V_p, V_s, and V_p/V_s models at different depths are shown in Figure 7. A cross section through the model is shown in Figure 8. The V_p and V_s models are displayed using the percentage deviation from the initial 1-D model in order to highlight changes from the "average" structure. The percent changes in the V_p/V_s model were relatively small, so the absolute value of V_p/V_s is plotted instead. Checkerboard tests reveal that we are sensitive to structures with dimensions larger than about 4 km, as discussed in section 3. Therefore, smaller-scale features are not discussed here to avoid the possibility of interpreting artifacts.

Figure 6. (first and second columns) V_P and (third and fourth columns) V_S checkerboard recovery tests for 4 km sized checkers at $Z = 2$ km, 5 km, 10 km, and 15 km and corresponding contoured normalized correlation coefficients for a sliding window 8 km across. The velocity perturbations are displayed on a color scale from −5% (red) to +5% (blue), and the correlation coefficients are colored from −1 (blue) to +1 (red). Correlation coefficients are contoured every 0.1 units with the 0.0 value contour dashed and the 0.5 value contour in bold. Regions of the model which are well recovered have correlation coefficients of 0.5 or higher.
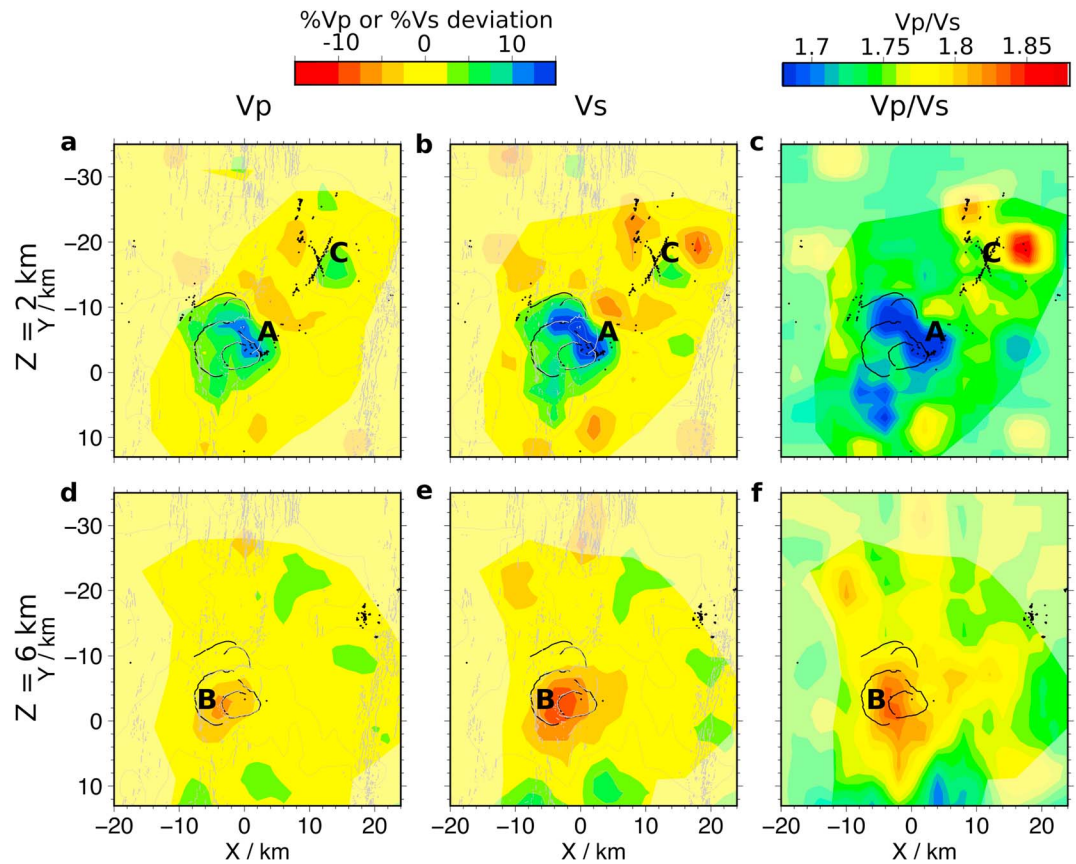
Figure 7. Depth slices at (a–c) 2 km bsl and (d–f) 6 km bsl through the final V_p (Figures 7a and 7d), V_s (Figures 7b and 7e), and V_p/V_s ratio (Figures 7c and 7f) velocity models. The V_p and V_s models are plotted as percentage deviations from the initial 1-D model, and the V_p/V_s ratio model is plotted as the absolute values. The area at each depth which is well recovered in the checkerboard tests is plotted in full color. The letters A, B, and C indicate the main anomalies discussed in the text, and the thin black lines are the outlines of the Askja caldera faults. Earthquakes within 1 km of the displayed depth are indicated by black dots.
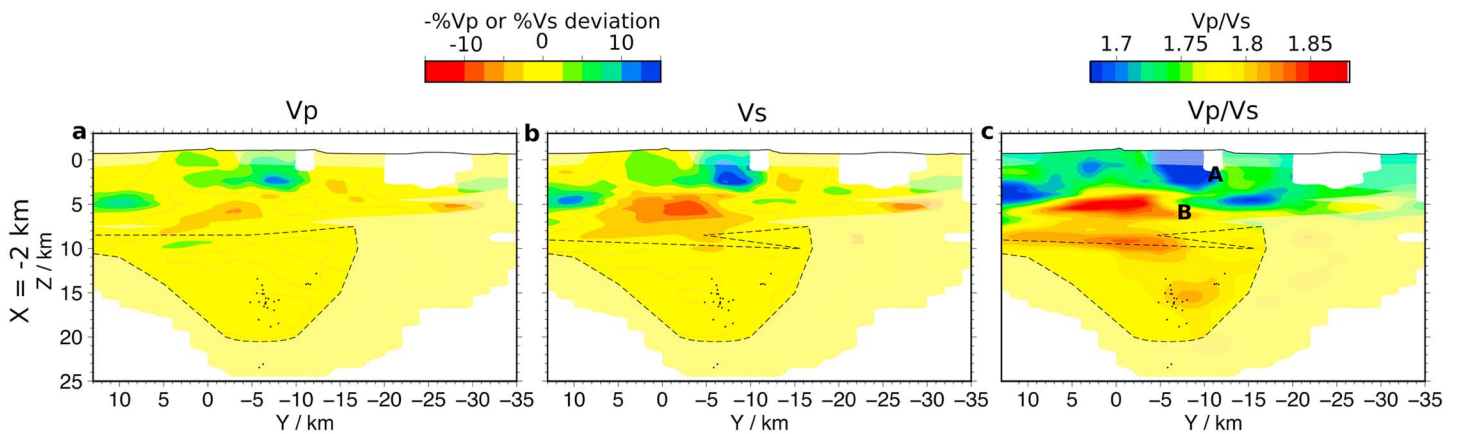

Figure 8. Cross sections along $x = -2$ km through the final (a) V_p, (b) V_s, and (c) V_p/V_s ratio velocity models. The V_p and V_s models are plotted as percentage deviations from the initial 1-D model, and the V_p/V_s ratio model is plotted as absolute values. The letters A and B indicate the main anomalies as discussed in the text. Earthquakes within 1 km of the displayed section are indicated by black dots. Regions in which the recovery of low-velocity bodies is good although the cross correlation value is below 0.5 is indicated by the dashed lines.

4.1. Upper Crust

The upper crust is highly heterogeneous in V_p, V_s, and V_p/V_s. Near the surface ($z = 2$ km, Figures 7a–7c), high-V_p and V_s anomalies and low-V_p/V_s ratios are present in a ring around the Askja caldera, predominantly located on the eastern side, extending to 4 km depth (anomaly A). To the northeast of Askja, around Herðubreið, a circular high-V_p/V_s anomaly stretches along rift (anomaly C). Although not well developed in the V_p model, a strong low-V_s anomaly matches the location of the V_p anomaly. Between the caldera and Herðubreið there is a region of low V_p and V_s, with no associated V_p/V_s anomaly.

Deeper in the upper crust ($z = 6$ km, Figures 7d–7f), the V_p model shows only subdued anomalies. In contrast, the V_s and V_p/V_s models exhibit strong anomalies (low V_s, high V_p/V_s) beneath Askja caldera (anomaly B). The anomaly is wider along rift (parallel to the y axis) than across it. Other low-V_s anomalies are present along rift, coincident with a region which shows a small increase in the V_p/V_s ratio relative to the 1-D model. Cross sections (Figure 8) show that the low-V_s region extends from 3.5 km to ~10 km depth. However, the region of significant low V_s ends at 7.5 km depth. In the V_p/V_s model, two anomalies are observed: a strong positive V_p/V_s anomaly centered at 5 km depth, slightly to the south of the V_s anomaly, and a weaker anomaly centered at 9 km depth slightly to the east of the other V_p/V_s anomaly (Figure 8).

4.2. Lower Crust

The lower crust ($Z > 8$ km) shows lower magnitude velocity anomalies than the upper crust, likely due to lower resolution in this region than in the upper crust. A region of slightly elevated V_p/V_s extends into the lower crust (Figure 8) and is focused at the location of the deep clusters of earthquakes (supporting information Movie S1). The strongest of the deep V_p/V_s anomalies is located around the Vaðalda cluster (supporting information Movie S1), which is also associated with a strong low-V_s anomaly (supporting information Movie S2).

5. Synthetic Tests: Realistic Earth Structure

Synthetic tests such as checkerboard tests are useful in order to test the minimum size of anomalies adjacent to each other which are likely to be resolved in different areas of the model. However, they are not realistic Earth structures, and so we do not gain full insight into how the observed anomalies may relate to real changes in the Earth's seismic velocity. We therefore use synthetic models which either relate to observed structures seen in the model or to idealized Earth structure in order to test the sensitivity of the model to these anomalies.

Synthetic velocity models are generated on grids of the same size as the grid used in the actual inversion with the same grid spacing. We apply a ±4.35% V_p and ±13.05% V_s perturbation to the initial 1-D velocity model. This results in a ∓10% V_p/V_s perturbation. Traveltime look-up tables are generated for the synthetic model using the same finite-difference algorithm. Next we calculate traveltimes for each earthquake used in the actual inversion to each station which detected the original earthquake. The synthetic traveltimes are then inverted for the model structure using the same 1-D velocity model and inversion procedure as those used for the inversion of real data.

Three synthetic tests are presented here: further tests are summarized in the supporting information.

5.1. Lower Crustal Low-Velocity Anomaly

We test the sensitivity of the inversion to low-velocity anomalies in the lower crust by generating a $6 \times 6 \times 3$ km low-velocity volume centered at ($x,y,z = 10,-15,14$) which has no earthquakes within it (Figure 9).

Recovered amplitudes and spatial coverage of the perturbations to the input model are significantly smaller than those in the synthetic model. We image no perturbations in the V_p model, but in the V_s and V_p/V_s models an anomaly is imaged, although it has a significantly lower amplitude than the applied velocity perturbation.

5.2. Upper and Lower Crustal Low-Velocity Anomaly

We test the ability of our method to recover two of the key results from the inversion by creating synthetic models with two low-velocity bodies. An upper crustal low-velocity body is created with approximately the
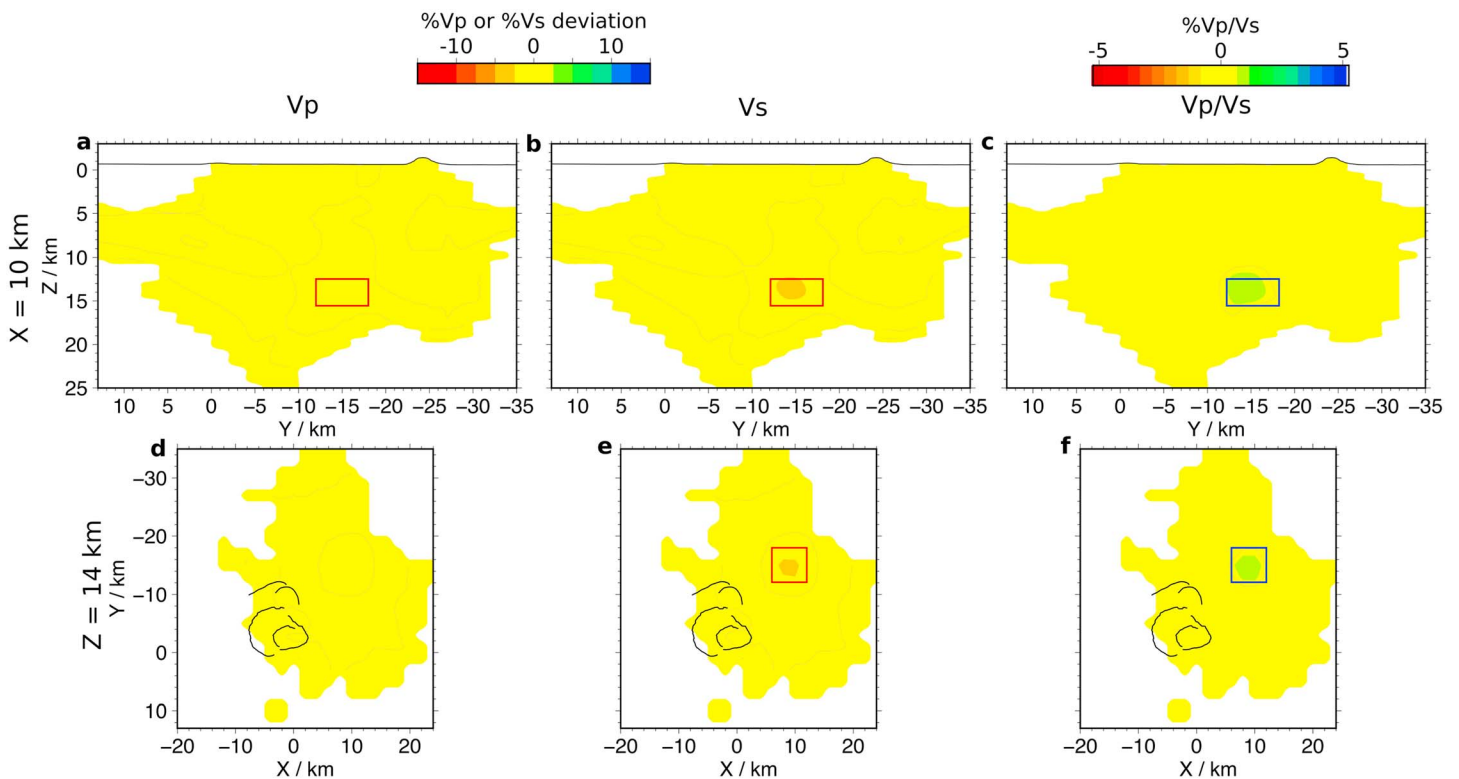
Figure 9. Synthetic test showing the recovery of a low-velocity anomaly centered at $(x,y,z = 10,-15,14)$. (a–c) The cross section through $x = 10$ km and (d–f) a depth slice through the models at 14 km bsl. The V_p, V_s, and V_p/V_s ratio models are plotted in Figures 9a and 9d, 9b and 9e, and 9c and 9f, respectively. The V_p and V_s models are plotted as percentage deviations from the initial 1-D model, and the V_p/V_s ratio model is plotted as absolute values. The synthetic model used to generate the traveltimes is indicated by the red or blue box outlining the applied anomaly. A red box indicates a low-velocity perturbation in V_p or V_s, and a blue box indicates a positive perturbation in V_p/V_s. The thin black lines are the outlines of the Askja caldera faults.

size and shape of anomaly B $(x,y,z = -4,0,7)$. In the lower crust we generate a slightly larger low-velocity body around the deep cluster of earthquakes beneath Askja $(x,y,z = 0,-8,16)$.

Recovery of the synthetic model (Figure 10) reveals that the recovered amplitudes of the anomalies are lower than the anomalies in the synthetic model. This is especially apparent in the recovery of the low-velocity body in the lower crust using P waves. In this case, the velocity anomaly is not imaged. This is due to the higher number of S wave picks than P wave picks from earthquakes in this area, due to attenuation of the high-frequency P wave [*Greenfield and White*, 2015].

There is significant smearing between the upper and lower crustal anomalies, mostly in the recovery of the V_s structure. This is because there are few raypaths which cross horizontally between 15 and 10 km depth. Instead, rays mostly travel subvertically, producing the significant smearing between the low-velocity bodies.

The recovery of the V_p/V_s structure of the upper body is significantly smaller than the imposed anomaly (maximum recovered amplitude is +3% compared to the imposed anomaly of +10%). Interestingly, the recovered amplitudes from the lower crustal anomaly are the same as those of the upper crustal body, suggesting equal sensitivity to V_p/V_s variations in the lower and upper crust.

5.3. Upper Crustal Low-Velocity Body With High-Velocity Ring

Geodetic studies of Askja have interpreted the observed subsidence as caused by a deflating magma body located in the center of the largest caldera in Askja, at a depth of 2 km bsl [*de Zeeuw-van Dalfsen et al.*, 2012]. Such a body would be seismically visible as a region of significantly lower velocities in the center of the caldera. Results show that the Askja caldera is surrounded by high seismic velocities (Figure 7) so imaging such a shallow low-velocity body could be difficult. To test this, we have produced three synthetic models. The first has a 6 km wide and 4 km thick low-velocity body centered at $(x,y,z = -4,-3,2)$ within a 6 km wide
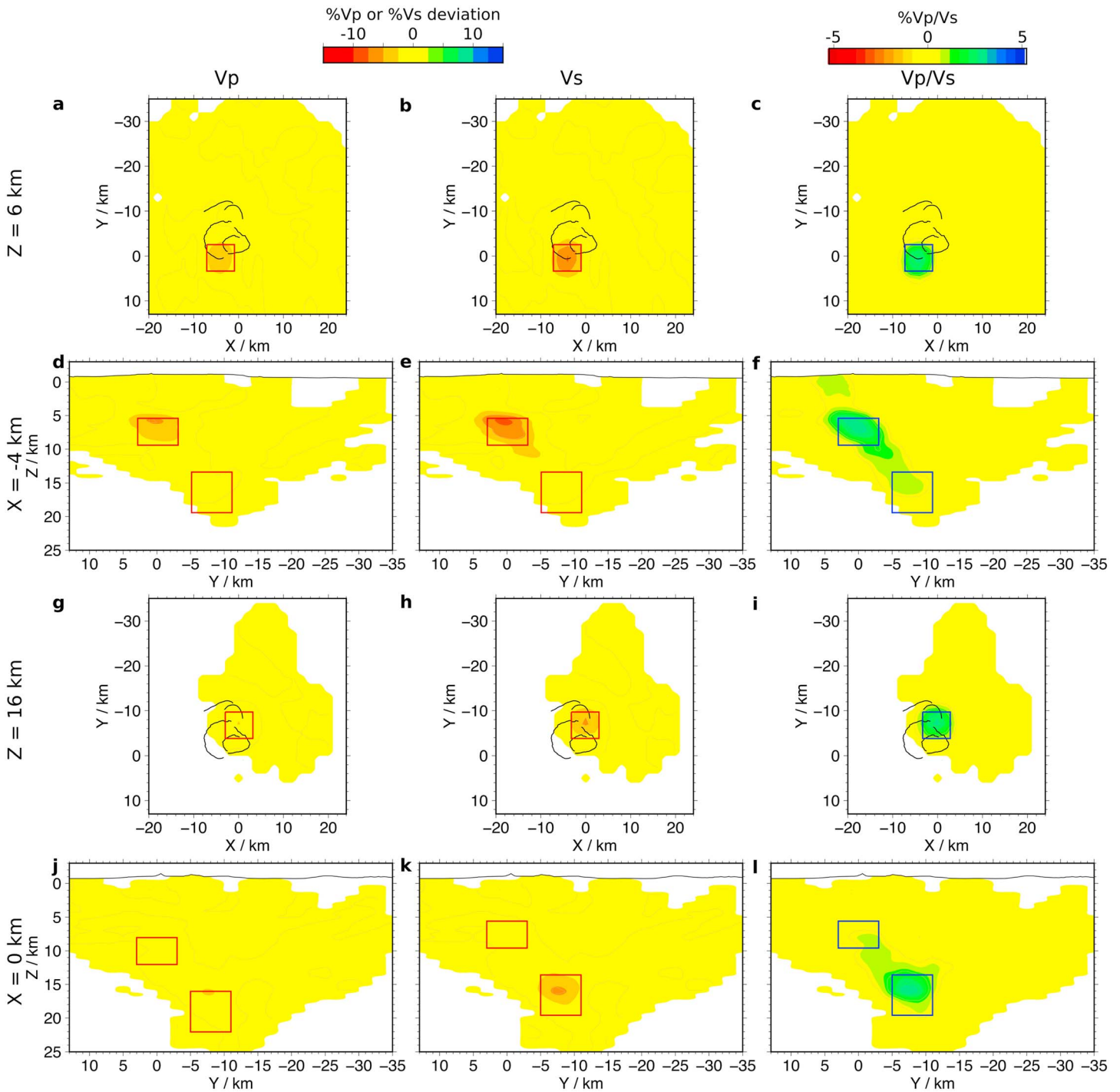
Figure 10. As Figure 9 but for a synthetic test recovering a low-velocity body at $(x,y,z = -4,0,7)$ and another centered at $(x,y,z = 0,-8,16)$. (a–c) Sections through $z = 6$ km and (d–f) sections through $x = -4$ km. (g–i) Section through $z = 16$ km and (j–l) sections through $x = 0$ km.

high-velocity ring (Figures 11a–11f). The second is 2 km thick (Figures 11g–11l), and the third has a 3 km wide and 2 km thick low-velocity region within a high-velocity ring 9 km wide (Figures 11m–11r).

The V_p and V_s recovery of the low-velocity body in the first model is good, although the high-velocity body is barely visible in the V_p model (Figures 11a and 11d). The low-velocity body is stronger toward the bottom of the imposed perturbation because the density of rays toward the upper edge of the model is significantly worse than at greater depths, especially within the caldera. The recovery of the V_p/V_s structure is not as good
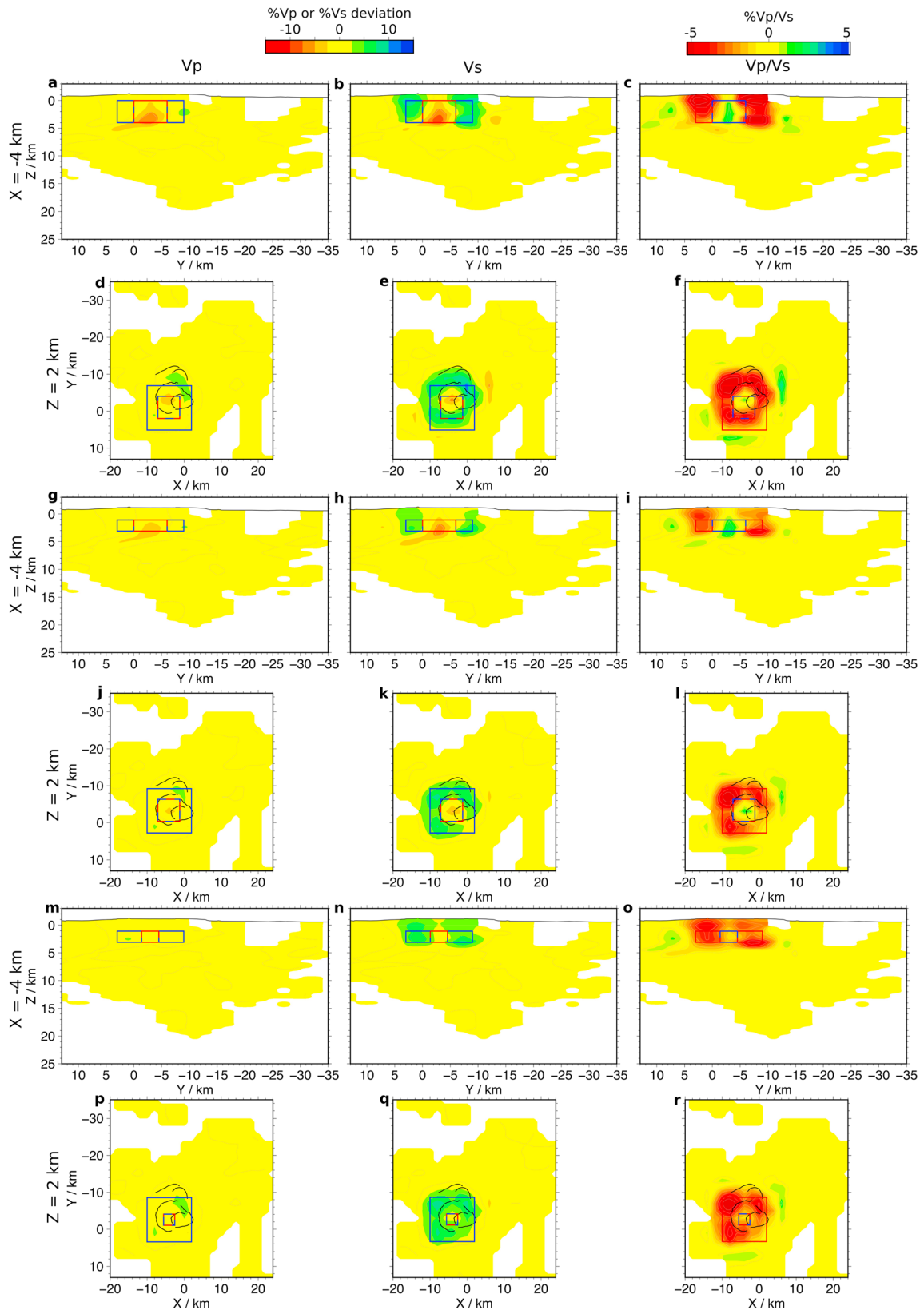
Figure 11. As Figure 9 but for a synthetic test recovering a low-velocity body (LVB) at (−4,−3,2) surrounded by a high-velocity ring. (a–f) A 6 km wide and 4 km thick LVB surrounded by a high-velocity ring 6 km thick. (g–l) A 6 km wide and 2 km thick LVB surrounded by a 6 km thick high-velocity ring. (m–r) A 3 km wide and 2 km thick LVB with a 9 km thick high-velocity ring. In all sets of panels, Figures 11a–11c show sections cut through x = −4 km; Figures 11d–11o are cut through z = 2 km.

as recovery of the V_p and V_s structure. The low-V_p/V_s anomalies are recovered with unusually strong anomalies, with similar amplitudes to the initial perturbations (Figure 11f). The recovery of the high-V_p/V_s region within the center of the low-V_p/V_s ring is very poor, with no visible changes to the initial 1-D model in either the V_p, V_s, or V_p/V_s models.

The second model, with a thinner initial anomaly is not recovered quite as well (Figures 11g–11l). A similar pattern is observed to that of the first model, with good recovery of the low-velocity body in the V_p and V_s models, especially near the bottom of the imposed perturbation. In the V_s model the center of the low-velocity body is at ~3 km depth rather than at 2 km depth, reflecting the lower density of rays near the surface. The high-velocity ring is well imaged in the V_s model but is poorly visible in the V_p model. The recovery of the V_p/V_s anomaly is the same as for the previous model. The low-velocity ring is recovered well, although with smaller amplitudes than in the first model. The high-V_p/V_s ratios are not visible in the recovered model.

The final model has very poor recovery of the low-velocity body (Figures 11m–11r), indicating that the minimum resolution is larger than 3 km, similar to that deduced from the checkerboard tests. The high-velocity ring is recovered well in the V_s and V_p/V_s models but less well in the V_p model.

6. Discussion

6.1. Herðubreið Low-Velocity Anomaly—Anomaly C

Anomaly C, a region of low V_s and high V_p/V_s at shallow (2 km bsl) depths near Herðubreið (Figure 7) would usually be interpreted as a region of high temperatures and/or melt given the volcanic setting. However, there is a lack of recent eruptive products, and there is no surface indication of high temperatures at shallow depths such as geothermal activity. Additionally, contrary to what is expected for a region of high temperatures, the V_p and V_s models are not correlated (Figure 7).

High V_p/V_s are often found in saturated sediments because fluids have a higher bulk modulus than gases [*Nicholson and Simpson*, 1985; *Lees*, 2007]. Increasing the crack density can also increase the V_p/V_s ratio [*Wang et al.*, 2012], provided that the solid is saturated. In the Herðubreið region both mechanisms could be acting to increase the V_p/V_s ratio. The region is the most seismically active area close to Askja, with a series of northeast-southwest trending left-lateral faults accommodating differential plate spreading between two volcanic systems in a bookshelf sense [*Green et al.*, 2014]. It must therefore be pervasively fractured. There are also a large number of springs in the area that flow all year round. These suggest that the region is fluid saturated.

In the South Iceland Seismic Zone (SISZ, Figure 1), a region which is tectonically analogous to the Herðubreið region [*Einarsson*, 1991], *Tryggvason et al.* [2002] observed a similar pattern in the seismic velocity structure. This suggests that this pattern of high V_p and high V_p/V_s may be common to all the seismically active and therefore pervasively fractured regions of the Icelandic crust.

6.2. The Upper Crust Beneath Askja Caldera—Anomaly A

In the shallowest portion of the crust beneath Askja (depth < 3 km bsl) the crust is predominantly faster than the initial 1-D model in a region surrounding the Askja central volcano. High-V_p crust in a volcanic setting is usually interpreted to be the result of an intrusive body [*Arnott and Foulger*, 1994; *Lees*, 2007]. However, the V_p/V_s ratio of gabbro or dolerite is above 1.8 [*Christensen*, 1996], whereas this region has a lower V_p/V_s ratio than the 1-D model, with a value of ~1.7 (Figure 7). This suggests that either the V_p/V_s ratio is being reduced by the presence of a gas or that the composition of the intrusions is not basaltic.

Felsic melts have been directly sampled and imaged beneath the Krafla central volcano [*Zierenberg et al.*, 2013; *Schuler et al.*, 2015], and rhyolitic eruptions, although rare, are found elsewhere in Iceland. However, the majority of the volcanism from Askja is basaltic in composition [*Thordarson and Höskuldsson*, 2008], and studies of exhumed central volcanoes in eastern Iceland indicate that the bulk of the subsurface is basaltic [*Thorarinsson and Tegner*, 2009]. It therefore seems likely that the intrusive complexes beneath Askja, which cause the high seismic velocities observed, are gabbroic, and the observed low-V_p/V_s ratio is due to a phase transition from water to steam [*Ito et al.*, 1979]. This is similar to changes in V_p/V_s observed in other geothermal regions around the world [e.g., *Chatterjee et al.*, 1985]. Beneath central volcanoes in Iceland, because they have a high geothermal gradient, the water to steam transition occurs very shallow in the crust. Under Krafla, which
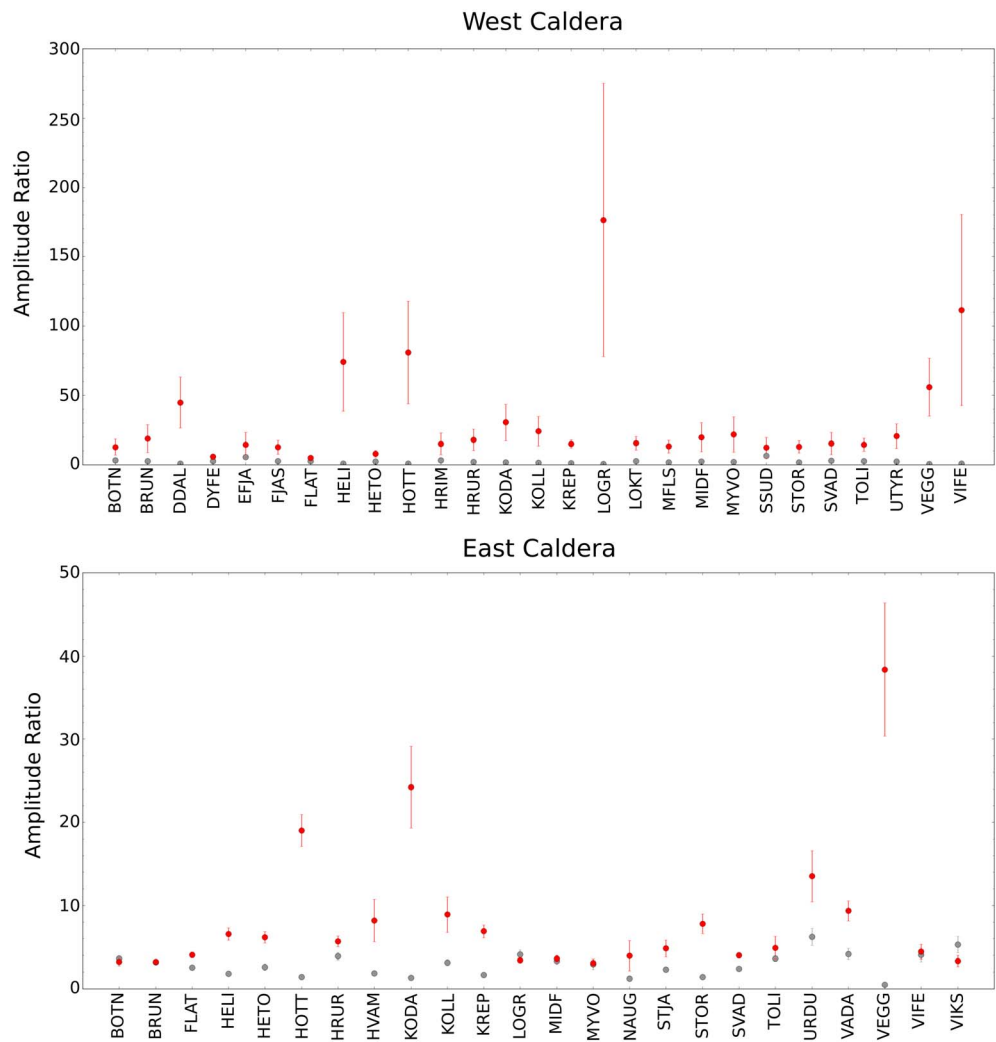
Figure 12. The attenuation of rays which pass across the caldera. Plots show the mean ratio between the amplitude observed at the labeled station and that recorded by stations which are on the opposite side of the caldera (red circles), or other stations (gray circles). Rays from earthquakes on the west side of the caldera (top panel) and earthquakes on the east side of the caldera (bottom panel) which cross the caldera have significantly higher ratios than those which do not; indicating that the region in the caldera has higher attenuation than the surrounding crust.

is actively exploited for geothermally derived hot water and power, the steam transition occurs at ~2 km bsl, similar to the depth of the low-V_p/V_s ratios below Askja [*Halldórsdóttir et al.*, 2010].

6.2.1. Presence of a Low-Velocity Body Shallow in the Crust

Earthquakes in two clusters to the east and west of Askja caldera show a pronounced drop in the recorded amplitude between rays which cross the caldera and rays which do not (Figure 12). This is observed after applying corrections for focal mechanism, regional attenuation ($Q = 30$), instrument response, and geometrical spreading. A highly attenuating region at a depth of < 3 km bsl could cause the amplitude drop, as observed farther north at Krafla [*Einarsson*, 1978]. It might be expected that any highly attenuating body would also be associated with the presence of a low-velocity body as high temperatures can cause both effects. However, we see no evidence for a region of low velocities in the tomographic model, and the observed residuals on rays which cross the caldera (Figure 10) do not show a delay, as would be expected from crossing a low-velocity region.

Part of the difficulty in observing a shallow low-velocity zone is the ring of high-velocity material around the caldera. This could reduce any signal from a potential low-velocity zone within the caldera. Additionally, at

shallow depths (<3 km bsl), the sensitivity of seismic tomography is often lower as a result of the station spacing being larger than the imaged depths. In this study this is certainly the case because the station spacing is ~5 km. Synthetic tests (Figure 11) suggest that any low-velocity body in the shallow crust beneath Askja would only be imaged if it had a volume greater than 15 km^3. This is significantly smaller than that inferred for the shallow magma chamber from geodetic measurements (60 km^3) [*Pagli et al.*, 2006] but sufficiently large to be the source of the 1875 rhyolitic eruption from Askja (0.321 km^3 dense rock equivalent) [*Carey et al.*, 2010] and cause the observed long-term subsidence. A denser seismic network within the caldera itself, in combination with active sources, would be required to illuminate the shallow structure of the caldera and to image the highly attenuating region.

6.3. The Base of the Upper Crust—Anomaly B

At a depth of 6 km bsl, the most prominent feature in the tomographic results is the pair of large low-V_p, low-V_s, and high-V_p/V_s anomalies directly beneath Askja (Figure 7). The deeper anomaly is poorly expressed in the V_p and V_s models because of the lower resolution at this depth (Figure 4). It is likely that it does not extend as far to the west as is observed in Figure 6i because part of the V_p/V_s signal in this area is the result of an increase in V_p. Synthetic tests (Figure 10) reveal that the observed elongation along the rift is unlikely to be a real feature, as this appeared in the recovered model, despite a square low-velocity body being used as an input in the synthetic model. The amplitude of the anomalies is likely to be underestimated given the damping and smoothing which has been applied to the model and, as a consequence of this, the extent of the anomalies is likely to be overestimated.

At depths of 5–9 km in the crust, pervasive fracturing is unlikely to be the cause of the observed changes in seismic velocity. Therefore, we interpret these results to be caused by a region of high temperatures and/or melt. Similar low-velocity bodies have been reported under many volcanoes around the world and have been interpreted as the primary storage region for melt in the crust for each volcano [e.g., *Cardaci et al.*, 1993; *Lin et al.*, 2014; *Ohlendorf et al.*, 2014; *De Siena et al.*, 2014]. Further evidence for the presence of high temperatures is that these regions of the model have no earthquakes within them. Presumably, this is because the relaxation time for the country rock in this area is so short that stresses cannot build up to induce brittle failure. Bodies of this size (~100 km^3) are unlikely to be composed entirely of melt but are likely to represent heavily intruded regions of the crust with melt sitting in lenses at low melt fractions or within a mush. Using the relationship between seismic velocity and melt fraction of *Caricchi et al.* [2008], we estimate an average melt fraction of ~10%, similar to that reported beneath Kīlauea's East Rift Zone [*Lin et al.*, 2014]. It should be noted that because of the smoothing applied during the tomographic inversion, these are minimum estimates of the melt fraction.

Geophysically imaged magma storage regions in Iceland, such as those beneath Krafla [*Einarsson*, 1978; *Brandsdóttir et al.*, 1997], Hengill [*Toomey and Foulger*, 1989], Katla [*Gudmundsson et al.*, 1994], and Eyjafjallajökull [*Sigmundsson et al.*, 2010], are all centered at depths less than 3 km bsl. Deeper chambers do occur, such as that inferred beneath Hekla and Torfajökull (greater than 14 km depth) [*Soosalu and Einarsson*, 2004], but Askja is alone in having a region of melt at a depth of 5–9 km bsl. However, this may be due to the imaging techniques used. Local earthquake tomography is very dependent on the locations of the background seismicity, and many volcanoes in Iceland do not have sufficiently deep earthquakes to image bodies in the midcrust. This can be seen in the study by *Schuler et al.* [2015], which, using similar methods to this study, could not reliably image seismic velocity anomalies below a depth of 5 km bsl because much of the local seismicity occurred shallower than 5 km bsl. We are fortunate in this study of Askja in being able to use arrivals from several clusters of earthquakes occurring at depths of 12–22 km [*Greenfield and White*, 2015], deeper than the magma storage regions.

6.4. Lower Crust

The lower crust beneath Askja does not show the large variations in seismic velocity which are observed in the upper crust. However, synthetic tests (Figure 10) show that around the earthquakes in the lower crust we have the same sensitivity to changes in the seismic velocity. It is these regions around the lower crustal earthquakes (Figure 2) which have reduced seismic velocities and higher V_p/V_s ratios than the surrounding crust (Figure 8 and supporting information Movie S1) suggesting the presence of high temperatures and melt. This matches inferences from highly accurate locations of the seismicity in the lower crust [*Key et al.*,
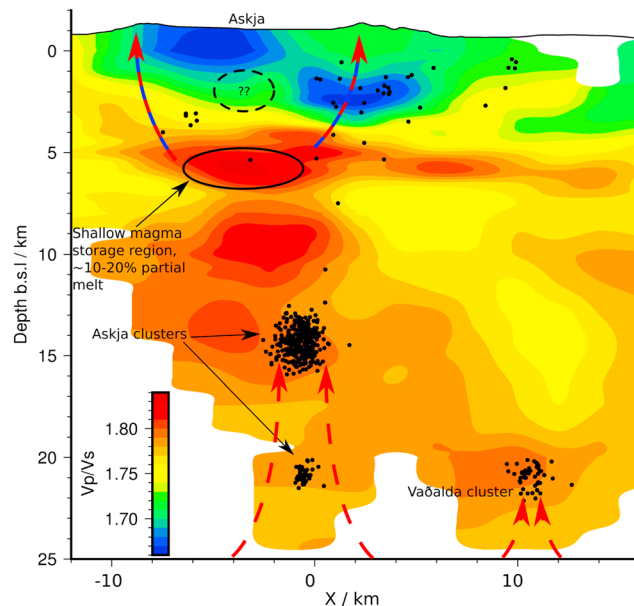
Figure 13. Interpretation of the velocity structure and seismicity parallel to the plate spreading direction beneath Askja. The $y = -5$ km section (see Figure 2 for location) is plotted through the final V_p/V_s model. The model is colored according to the color bar shown in the bottom left of the figure. Seismicity located within 2 km of $y = -5$ km is indicated by the black circles. The imaged magma storage body in the upper crust is outlined by the solid black line. The maximum possible size of any shallow low-velocity body centered at 2 km depth is indicated by the dashed black oval. Dashed red lines show the potential flow of melt through the crust.

2011a, 2011b; *Greenfield and White*, 2015]. Since the magnitude of the change in seismic velocity is lower than those in the upper crust, this suggests that the melt occurs at lower melt fractions and is more distributed throughout the seismogenic regions in the lower crust.

The cluster of earthquakes to the east of Askja, beneath the mountain Upptyppingar (see Figure 1 for location), is associated with the intrusion of an inclined dike into the crust in 2007–2008 [*White et al.*, 2011; *Martens and White*, 2013]. These earthquakes are not associated with any changes in the seismic velocity. Modeling of the ground deformation indicates that there was a maximum 1 m of opening of the dike and the intrusion of 0.045 km^3 of melt [*Hooper et al.*, 2011]. In contrast to the other clusters of deep earthquakes, the Upptyppingar seismicity is not persistent and died away relatively quickly after the dike had been intruded. This means that there is not as much melt in this region of the crust, and any effect on the tempera-

ture of the crust was temporary and over such a small volume that it did not affect the seismic velocity over a sufficiently large volume to be resolvable. The other clusters are all associated with high-V_p/V_s ratios, indicating the presence of high temperatures over a long period of time and a sufficiently large volume to appreciably alter the seismic velocity.

6.5. The Magmatic Plumbing System Beneath Askja Central Volcano

The distribution of earthquakes and seismic velocity anomalies beneath Askja are suggestive of a complex magmatic plumbing system with melt distributed throughout the crust (Figure 13 and supporting information Movies S1 and S2). Melt is currently being actively intruded into a number of discrete locations in the midcrust, rather than at a single location beneath the central volcano. These regions must have been active for a relatively long time, as short-lived intrusion events for which we know the dates do not have an associated seismic velocity perturbation.

Despite observing a high-V_p/V_s "network" which links the upper and lower crust (supporting information Movies S1 and S2), synthetic tests suggest that such observations could be due to the inherent smoothing in the model, applied during the inversion. Nevertheless, such melt pathways must have occurred in the past, because a pair of large low-velocity bodies, which we interpret to be heavily intruded regions of the crust, is obvious at the base of the upper crust, straddling the brittle-ductile transition at 7 km bsl. These could have first been formed by the intrusion of sills, possibly by the deflection of dikes at a rheological boundary [*Kavanagh et al.*, 2015]. Once intruded the sill can act as a locus for successive dikes, thereby creating a heavily intruded region of the crust [*Menand*, 2011].

Shallower magmatic bodies, such as those imaged beneath Krafla [*Einarsson*, 1978; *Schuler et al.*, 2015] and inferred beneath Askja [*de Zeeuw-van Dalfsen et al.*, 2013], are likely to be formed close to the beginning of an eruption and to cool quickly afterward. Because of this, they are likely to play a less important role in how the Icelandic crust is built than larger magmatic bodies that exist deeper in the crust.

Only a small proportion of the melt injected into the crust is extruded at the surface, with the rest freezing in situ to generate the bulk of the middle and lower crust. The low-velocity regions and active seismicity we record deeper than 9 km represent melt ponding in the deeper crust.

7. Conclusions

We have generated a large catalog of earthquakes with manually refined arrival times for both P and S waves. We have used this catalog to invert simultaneously for the earthquake locations and the velocity structure beneath Askja, a central volcano in central Iceland. Results show three main seismic velocity anomalies in the upper crust:

1. A region of high-V_p, high-V_s, and low-V_p/V_s ratio in a ring around Askja at a depth of 2 km bsl, interpreted to be due to a high seismic velocity intrusive complex in the shallow crust.
2. A region of high-V_p and high-V_p/V_s ratio at a depth of 2 km bsl around the table mountain Herðubreið caused by the pervasive fracturing of this seismically active region.
3. A region of low-V_p, low-V_s, and high-V_p/V_s ratio with a total volume of ~100 km^3 directly beneath Askja, concentrated at two depths (5 and 9 km bsl), interpreted to be the primary melt storage regions in the upper crust.

In the lower crust, synthetic testing shows that we have the sensitivity to detect regions of anomalous seismic velocity. Although, because of the clustered nature of the seismicity, the coverage is not as good as in the upper crust. We have shown that the regions around areas containing lower crustal earthquakes have low V_s and high V_p/V_s. This suggests that these regions are areas of significant melt storage as well as regions where melt is being actively transported.

The sensitivity in the shallowest part of the upper crust beneath Askja has been tested using synthetic tests. These indicate that the maximum size of any potential magma chamber at this depth is ~15 km^3 which, although large enough to source the eruption in Askja in March 1875 and cause the observed subsidence of the caldera, is small relative to the much larger low-velocity bodies imaged deeper in the crust. Although such large bodies are unlikely to spend much of their time as fully molten entities, they probably act as the final storage and equilibration depth for any eruption sourced from beneath Askja. These bodies are likely to exist beneath many Icelandic volcanoes but due to the difficulties in imaging them have yet to be mapped in other locations.

References

Ágústsdóttir, T., J. Woods, T. Greenfield, R. G. Green, R. S. White, T. Winder, B. Brandsdóttir, S. Steinthórsson, and H. Soosalu (2016), Strike-slip faulting during the 2014 Bárðarbunga-Holuhraun dike intrusion, central Iceland, *Geophys. Res. Lett.*, *43*, 1495–1503, doi:10.1002/2015GL067423.

Alfaro, R., B. Brandsdóttir, D. P. Rowlands, R. S. White, and M. T. Gudmundsson (2007), Structure of the Grimsvotn central volcano under the Vatnajokull icecap, Iceland, *Geophys. J. Int.*, *168*(2), 863–876.

Arnott, S. K., and G. R. Foulger (1994), The Krafla spreading segment, Iceland 1. Three-dimensional crustal structure and the spatial and temporal distribution of local earthquakes, *J. Geophys. Res.*, *99*, 23,801–23,825, doi:10.1029/94JB01465.

Beyreuther, M., R. Barsch, L. Krischer, T. Megies, Y. Behr, and J. Wassermann (2010), ObsPy: A Python toolbox for seismology, *Seismol. Res. Lett.*, *81*(3), 530–533, doi:10.1785/gssrl.81.3.530.

Brandsdóttir, B. (1992), Historical accounts of earthquake associated with eruptive activity in the Askja volcanic system, *Jökull*, *42*, 1–9.

Brandsdóttir, B., W. Menke, P. Einarsson, R. S. White, and R. K. Staples (1997), Faroe-Iceland ridge experiment 2. Crustal structure of the Krafla central volcano, *J. Geophys. Res.*, *102*, 7867–7886, doi:10.1029/96JB03799.

Cardaci, C., M. Coviello, G. Lombardo, G. Patane, and R. Scarpa (1993), Seismic tomography of Etna volcano, *J. Volcanol. Geotherm. Res.*, *56*(4), 357–368.

Carey, R. J., B. F. Houghton, and T. Thordarson (2010), Tephra dispersal and eruption dynamics of wet and dry phases of the 1875 eruption of Askja Volcano, Iceland, *Bull. Volcanol.*, *72*(3), 259–278, doi:10.1007/s00445-009-0317-3.

Caricchi, L., L. Burlini, and P. Ulmer (2008), Propagation of P and S-waves in magmas with different crystal contents: Insights into the crystallinity of magmatic reservoirs, *J. Volcanol. Geotherm. Res.*, *178*(4), 740–750, doi:10.1016/j.jvolgeores.2008.09.006.

Chatterjee, S. N., A. M. Pitt, and H. M. Iyer (1985), V_p/V_s ratios in the Yellowstone national park region, Wyoming, *J. Volcanol. Geotherm. Res.*, *26*, 213–230.

Christensen, N. I. (1996), Poisson's ratio and crustal seismology, *J. Geophys. Res.*, *101*, 3139–3156, doi:10.1029/95JB03446.

De Siena, L., G. Waite, S. Moran, S. Klemme, and C. Thomas (2014), Attenuation and scattering tomography of the deep plumbing system of Mount St. Helens, *J. Geophys. Res. Solid Earth*, *16*, 8223–8238, doi:10.1002/2014JB011372.

de Zeeuw-van Dalfsen, E., R. Pedersen, A. Hooper, and F. Sigmundsson (2012), Subsidence of Askja caldera 2000–2009: Modelling of deformation processes at an extensional plate boundary, constrained by time series InSAR analysis, *J. Volcanol. Geotherm. Res.*, *213–214*, 72–82, doi:10.1016/j.jvolgeores.2011.11.004.

de Zeeuw-van Dalfsen, E., H. Rymer, E. Sturkell, R. Pedersen, A. Hooper, F. Sigmundsson, and B. G. Ófeigsson (2013), Geodetic data shed light on ongoing caldera subsidence at Askja, Iceland, *Bull. Volcanol.*, *75*(5), 709, doi:10.1007/s00445-013-0709-2.

Drew, J., R. S. White, F. Tilmann, and J. Tarasewicz (2013), Coalescence microseismic mapping, *Geophys. J. Int.*, *195*(3), 1773–1785, doi:10.1093/gji/ggt331.

Einarsson, P. (1978), *S*-wave shadows in the Krafla caldera in NE-Iceland, evidence for a magma chamber in the crust, *Bull. Volcanol.*, *41*(3), 187–195.

Einarsson, P. (1991), Earthquakes and present-day tectonism in Iceland, *Tectonophysics*, *189*(1–4), 261–279, doi:10.1016/0040-1951(91)90501-I.

Font, Y., H. Kao, S. Lallemand, C.-S. Liu, and L.-Y. Chiao (2004), Hypocentre determination offshore of eastern Taiwan using the maximum intersection method, *Geophys. J. Int.*, *158*(2), 655–675, doi:10.1111/j.1365-246X.2004.02317.x.

Foulger, G. R., A. D. Miller, B. R. Julian, and J. R. Evans (1995), Three-dimensional V_p and V_p/V_s structure of the Hengill Triple Junction and Geothermal Area, Iceland, and the repeatability of tomographic inversion, *Geophys. Res. Lett.*, *22*, 1309–1312, doi:10.1029/94GL03387.

Green, R. G., R. S. White, and T. Greenfield (2014), Motion in the north Iceland volcanic rift zone accommodated by bookshelf faulting, *Nat. Geosci.*, *7*, 29–33, doi:10.1038/ngeo2012.

Green, R. G., T. Greenfield, and R. S. White (2015), Triggered earthquakes suppressed by an evolving stress shadow from a propagating dyke, *Nat. Geosci.*, *8*, 629–632, doi:10.1038/ngeo2491.

Greenfield, T., and R. S. White (2015), Building Icelandic igneous crust by repeated melt injections, *J. Geophys. Res. Solid Earth*, *120*, 1–14, doi:10.1002/2015JB012218.

Gudmundsson, O., B. Brandsdóttir, W. Menke, and G. Sigvaldason (1994), The crustal magma chamber of the Katla Volcano in South Iceland revealed by 2-D seismic undershooting, *Geophys. J. Int.*, *119*(1), 277–296, doi:10.1111/j.1365-246X.1994.tb00928.x.

Halldórsdóttir, S., H. Björnsson, A. K. Mortensen, G. Axelson, and Á. Guðmundsson (2010), Temperature model and volumetric assessment of the Krafla geothermal field in N-Iceland, *Proc. World Geotherm. Congr.*, *C*(April), 10.

Hartley, M. E., and T. Thordarson (2012), Formation of Öskjuvatn caldera at Askja, North Iceland: Mechanism of caldera collapse and implications for the lateral flow hypothesis, *J. Volcanol. Geotherm. Res.*, *227–228*, 85–101, doi:10.1016/j.jvolgeores.2012.02.009.

Hartley, M. E., and T. Thordarson (2013), The 1874–1876 volcano-tectonic episode at Askja, North Iceland: Lateral flow revisited, *Geochem. Geophys. Geosyst.*, *14*, 2286–2309, doi:10.1002/ggge.20151.

Hjartardóttir, Á. R., and P. Einarsson (2015), The interaction of fissure swarms and monogenetic lava shields in the rift zones of Iceland, *J. Volcanol. Geotherm. Res.*, *299*(October), 91–102, doi:10.1016/j.jvolgeores.2015.04.001.

Hole, J. A., and B. C. Zelt (1995), 3-D finite-difference reflection travel times, *Geophys. J. Int.*, *121*(2), 427–434, doi:10.1111/j.1365-246X.1995.tb05723.x.

Hooper, A., B. Ófeigsson, F. Sigmundsson, B. Lund, P. Einarsson, H. Geirsson, and E. Sturkell (2011), Increased capture of magma in the crust promoted by ice-cap retreat in Iceland, *Nat. Geosci.*, *4*(11), 783–786, doi:10.1038/ngeo1269.

Ito, H., J. DeVilbiss, and A. Nur (1979), Compressional and shear waves in saturated rock during water-steam transition, *J. Geophys. Res.*, *84*, 4731, doi:10.1029/JB084iB09p04731.

Kavanagh, J. L., D. Boutelier, and A. R. Cruden (2015), The mechanics of sill inception, propagation and growth: Experimental evidence for rapid reduction in magmatic overpressure, *Earth Planet. Sci. Lett.*, *421*, 117–128, doi:10.1016/j.epsl.2015.03.038.

Key, J., R. S. White, H. Soosalu, and S. S. Jakobsdóttir (2011a), Correction to "Multiple melt injection along a spreading segment at Askja, Iceland,", *Geophys. Res. Lett.*, *38*, L05301, doi:10.1029/2010GL046264.

Key, J., R. S. White, H. Soosalu, and S. S. Jakobsdóttir (2011b), Multiple melt injection along a spreading segment at Askja, Iceland, *Geophys. Res. Lett.*, *38*, L05301, doi:10.1029/2010GL046264.

Lees, J. M. (2007), Seismic tomography of magmatic systems, *J. Volcanol. Geotherm. Res.*, *167*, 37–56.

Lin, G., F. Amelung, Y. Lavallee, and P. G. Okubo (2014), Seismic evidence for a crustal magma reservoir beneath the upper east rift zone of Kilauea volcano, Hawaii, *Geology*, *42*(3), 187–190, doi:10.1130/G35011.1.

Lomax, A., J. Virieux, P. Volant, and C. Berge (2000), Probabilistic earthquake location in 3D and layered models: Introduction of a Metropolis-Gibbs method and comparison with linear locations, in *Advances in Seismic Event Location*, edited by C. H. Thurber and N. Rabinowitz, pp. 101–134, Kluwer Acad., Amsterdam.

Martens, H. R., and R. S. White (2013), Triggering of microearthquakes in Iceland by volatiles released from a dyke intrusion, *Geophys. J. Int.*, *194*(3), 1738–1754, doi:10.1093/gji/ggt184.

Menand, T. (2011), Physical controls and depth of emplacement of igneous bodies: A review, *Tectonophysics*, *500*(1–4), 11–19, doi:10.1016/j.tecto.2009.10.016.

Mitchell, M. A., R. S. White, S. W. Roecker, and T. Greenfield (2013), Tomographic image of melt storage beneath Askja Volcano, Iceland using local microseismicity, *Geophys. Res. Lett.*, *40*, 5040–5046, doi:10.1002/grl.50899.

Nicholson, C., and D. W. Simpson (1985), Changes in V_p/V_s with depth: Implications for appropriate velocity models, improved earthquake locations, and material properties of the upper crust, *Bull. Seismol. Soc. Am.*, *75*(4), 1105–1123.

Nunn, C., S. W. Roecker, K. F. Priestley, X. Liang, and A. Gilligan (2014), Joint inversion of surface waves and teleseismic body waves across the Tibetan collision zone: The fate of subducted Indian lithosphere, *Geophys. J. Int.*, *198*(3), 1526–1542, doi:10.1093/gji/ggu193.

Ohlendorf, S. J., C. H. Thurber, J. D. Pesicek, and S. G. Prejean (2014), Seismicity and seismic structure at Okmok Volcano, Alaska, *J. Volcanol. Geotherm. Res.*, *278–279*, 103–119, doi:10.1016/j.jvolgeores.2014.04.002.

Pagli, C., F. Sigmundsson, T. Arnadottir, P. Einarsson, and E. Sturkell (2006), Deflation of the Askja volcanic system: Constraints on the deformation source from combined inversion of satellite radar interferograms and GPS measurements, *J. Volcanol. Geotherm. Res.*, *152*(1–2), 97–108, doi:10.1016/j.jvolgeores.2005.09.014.

Paige, C. C., and A. M. Saunders (1982), LSQR: An algorithm for sparse linear equations and sparse least squares, *Trans. Math. Software*, *8*, 43–71.

Rawlinson, N., A. Fichtner, M. Sambridge, and M. K. Young (2014), Seismic tomography and the assessment of uncertainty, *Adv. Geophys.*, *55*, 1–76, doi:10.1016/bs.agph.2014.08.001.

Roecker, S. W. (2004), Joint inversion of gravity and arrival time data from Parkfield: New constraints on structure and hypocenter locations near the SAFOD drill site, *Geophys. Res. Lett.*, *31*, L12S04, doi:10.1029/2003GL019396.

Roecker, S. W., C. H. Thurber, K. Roberts, and L. Powell (2006), Refining the image of the San Andreas Fault near Parkfield, California using a finite difference travel time computation technique, *Tectonophysics*, *426*(1–2), 189–205, doi:10.1016/j.tecto.2006.02.026.

Sæmundsson, K. (1979), Outline of the geology of Iceland, *Jokull*, *29*, 7–28.

Schuler, J., T. Greenfield, R. S. White, S. W. Roecker, B. Brandsdóttir, J. M. Stock, J. Tarasewicz, H. Martens, and D. Pugh (2015), Seismic imaging of the shallow crust beneath the Krafla central volcano, NE Iceland, *J. Geophys. Res. Solid Earth*, *120*, 7156–7173, doi:10.1002/2015JB012350.1.

Sigmundsson, F., et al. (2010), Intrusion triggering of the 2010 Eyjafjallajökull explosive eruption, *Nature*, *468*(7322), 426–30, doi:10.1038/nature09558.

Sigmundsson, F., et al. (2015), Segmented lateral dyke growth in a rifting event at Bárðarbunga volcanic system, Iceland, *Nature*, *517*, 191–195, doi:10.1038/nature14111.

Soosalu, H., and P. Einarsson (2004), Seismic constraints on magma chambers at Hekla and Torfajökull volcanoes, Iceland, *Bull. Volcanol.*, *66*(3), 276–286.

Soosalu, H., J. Key, R. S. White, C. Knox, P. Einarsson, and S. S. Jakobsdóttir (2010), Lower-crustal earthquakes caused by magma movement beneath Askja volcano on the north Iceland rift, *Bull. Volcanol.*, *72*(1), 55–62, doi:10.1007/s00445-009-0297-3.

Thorarinsson, S. (1962), The eruption in Askja, 1961 A preliminary report, *Am. J. Sci.*, *260*, 641–651.

Thorarinsson, S. B., and C. Tegner (2009), Magma chamber processes in central volcanic systems of Iceland: Constraints from layered gabbro of the Austurhorn intrusive complex, *Contrib. Mineral. Petrol.*, *158*(2), 223–244, doi:10.1007/s00410-009-0379-4.

Thordarson, T., and A. Höskuldsson (2008), Postglacial volcanism in Iceland, *Jokull*, *58*, 197–228.

Thordarson, T., and G. Larsen (2007), Volcanism in Iceland in historical time: Volcano types, eruption styles and eruptive history, *J. Geodyn.*, *43*(1), 118–152, doi:10.1016/j.jog.2006.09.005.

Toomey, D. R., and G. R. Foulger (1989), Tomographic inversion of local earthquake data from the Hengill-Grensdalur central volcano complex, Iceland, *J. Geophys. Res.*, *94*, 17,497–17,510, doi:10.1029/JB094iB12p17497.

Tryggvason, A., S. T. Rögnvaldsson, and Ó. G. Flóvenz (2002), Three-dimensional imaging of the *P*- and *S*-wave velocity structure and earthquake locations beneath Southwest Iceland, *Geophys. J. Int.*, *151*(3), 848–866, doi:10.1046/j.1365-246X.2002.01812.x.

Vidale, J. (1988), Finite-difference calculation of travel times, *Bull. Seismol. Soc. Am.*, *78*(6), 2062–2076.

Wang, X.-Q., A. Schubnel, J. Fortin, E. C. David, Y. Guéguen, and H.-K. Ge (2012), High V_p/V_s ratio: Saturated cracks or anisotropy effects?, *Geophys. Res. Lett.*, *39*, L11307, doi:10.1029/2012GL051742.

Wessel, P., W. H. F. Smith, R. Scharroo, J. Luis, and F. Wobbe (2013), Generic Mapping Tools: Improved version released, *Eos, Trans. Am. Geophys. Union*, *94*(45), 409–410, doi:10.1002/2013EO450001.

White, R. S., J. Drew, H. R. Martens, J. Key, H. Soosalu, and S. S. Jakobsdóttir (2011), Dynamics of dyke intrusion in the mid-crust of Iceland, *Earth Planet. Sci. Lett.*, *304*, 300–312.

Zierenberg, R. A., et al. (2013), Composition and origin of rhyolite melt intersected by drilling in the Krafla geothermal field, Iceland, *Contrib. Mineral. Petrol.*, *165*(2), 327–347, doi:10.1007/s00410-012-0811-z.